BNL-224630-2023-JAAM

GRP-AEM-5

Gate-Tunable Multiband Transport in ZrTe5 Thin Devices

Y. Liu, Q. Li

To be published in "Nano Letters"

June 2023

Condensed Matter Physics and Materials Science Department

Brookhaven National Laboratory

U.S. Department of Energy

USDOE Office of Science (SC), Basic Energy Sciences (BES) (SC-22)

DISCLAIMER

Gate-tunable multiband transport in $ZrTe_5$ thin devices

Yonghe Liu[1,2$], Hanqi Pi[1,2$], Kenji Watanabe[3], Takashi Taniguchi[4], Genda Gu[5], Qiang Li[5,6], Hongming Weng[1,2], Quansheng Wu[1,2*], Yongqing Li[1,2*], Yang Xu[1,2*]

[1]Beijing National Laboratory for Condensed Matter Physics, Institute of Physics, Chinese Academy of Sciences, Beijing 100190, China

[2]School of Physical Sciences, University of Chinese Academy of Sciences, Beijing 100049, China

[3]Research Center for Functional Materials, National Institute for Materials Science, 1-1 Namiki, Tsukuba 305-0044, Japan

[4]International Center for Materials Nanoarchitectonics, National Institute for Materials Science, 1-1 Namiki, Tsukuba 305-0044, Japan

[5]Condensed Matter Physics and Materials Science Department, Brookhaven National Laboratory, Upton, New York 11973-5000, USA

[6]Department of Physics and Astronomy, Stony Brook University, Stony Brook, New York 11794-3800, USA

*Correspondence to: quansheng.wu@iphy.ac.cn; yqli@iphy.ac.cn; yang.xu@iphy.ac.cn

[$]These authors contributed equally: Yonghe Liu, Hanqi Pi.

Abstract: Interest in $ZrTe_5$ has been reinvigorated in recent years owing to its potential for hosting versatile topological electronic states and intriguing experimental discoveries. However, the mechanism of many of its unusual transport behaviors remains controversial, for example, the characteristic peak in the temperature-dependent resistivity and the anomalous Hall effect. Here, through employing a clean dry-transfer fabrication method under inert environment, we successfully obtain high-quality $ZrTe_5$ thin devices that exhibit clear dual-gate tunability and ambipolar field effects. Such devices allow us to systematically study the resistance peak as well as the Hall effect at various doping densities and temperatures, revealing the contribution from electron-hole asymmetry and multiple-carrier transport. By comparing with theoretical calculations, we suggest a simplified semiclassical two-band model to explain the experimental observations. Our work helps to resolve the long-standing puzzles on $ZrTe_5$ and could potentially pave the way for realizing novel topological states in the two-dimensional limit.

KEYWORDS: Zirconium pentatelluride, anomalous Hall effect, multiple-carrier transport, ambipolar field effect

The Zirconium pentatelluride $ZrTe_5$ is a layered van der Waals material and has been shown to host distinct topological states in the vicinity to a topological phase transition (TPT). In the monolayer form, it is proposed to be a large-gap quantum spin hall insulator (QSHI)[1], whereas compelling evidence is still lacking. There are many novel physical properties that have been discovered for the $ZrTe_5$ crystals, ranging from high electron mobilities (up to ~ 640,000 $cm^2V^{-1}s^{-1}$)[2], the chiral anomaly[3], three-dimensional quantum Hall effect[4], and various parameter driven TPT[5-11]. Among the characteristic transport properties of $ZrTe_5$, the peculiar resistance peak at a temperature T_p ~140 K was first observed about 40 years ago, concomitant with a sign reversal of the Hall and Seebeck coefficients happening across T_p [12]. However, later studies show contrasting behaviors with the peak occurring in a wide temperature range from ~ 0 and 180 K[4, 13, 14]. The exact value of T_p is highly dependent on the growth condition of the bulk crystals and can vary sample to sample. The origin of such resistance anomalies has been debated for a long time but still remained unclear. The formation of a charge density wave[15, 16], a polaronic model[17, 18], a semimetal-semiconductor transition[19], a Lifshitz transition[20, 21], or a TPT[6, 7, 10] has been proposed.

Meanwhile, we have noticed that T_p is generally smaller for $ZrTe_5$ single crystals grown by the flux method comparing with that grown by the chemical vapor transport (CVT) method[4, 14]. For some samples grown by the flux method (nearly stoichiometric), semiconducting behavior down to the lowest temperature has been observed ($T_p \approx 0$)[14, 22-26]. Another typical observation is a p-type Hall/Seebeck coefficient for $T > T_p$ and a n-type/multi-carrier behavior for lower temperatures ($T < \sim T_p$). It has been suggested that the amount of Te vacancies, which act as electron donors, could contribute to the different transport behaviors in the narrow-gap semiconductor $ZrTe_5$ [26]. However, without the ability to finely control the Te deficiency or charge doping, solid conclusions cannot be reached.

In-situ electrostatic gating has been widely used in van der Waals (vdW) materials to tune their charge densities and facilitate the understanding of a plethora of intriguing phenomena. In the early efforts of fabricating the thin gating devices of $ZrTe_5$, a main obstacle is the degradation of crystal quality during the sample preparation. High densities of p-type carriers and low mobilities (~10^{19} cm^{-3} and <~10^3 $cm^2V^{-1}s^{-1}$) are typically observed[27, 28]. Meanwhile, efficient gating can hardly be achieved[23, 28-30]. Here, we adopt a clean layer-by-layer dry-transfer fabrication method developed for vdW heterostructures in recent years (see Methods for more details). Thin $ZrTe_5$ flakes are mechanically exfoliated from the bulk crystals grown by the flux method[3]. The exposure to air or solvents are fully avoided during the device fabrication process, which helps maintain the intrinsic properties of the $ZrTe_5$ crystals. We also encapsulate the $ZrTe_5$ on both

sides with hexagonal boron nitrides (hBN), which further improve the sample quality and prevent sample degradation during loading into the cryostats[31].

In this study, electrical transport measurements with changing gate voltages, temperatures, and magnetic fields are performed. Unless otherwise specified, the data presented below are collected from one representative device (about 12 nm thick, with an optical image shown in Fig. 1b). It exhibits clear ambipolar field effects and realizes efficient dual-gate tunability with mobilities up to ~15,000 $cm^2V^{-1}s^{-1}$. The resistance peaks, occurring at temperature T_p, can be systematically controlled by the gate voltages. The T_p reaches its minimum near the charge neutrality and increases on electron and hole-doped sides asymmetrically. The Hall measurements suggest that the resistance peak does not need to correlate with the sign change of Hall resistance on the hole-doped side. The anomalous Hall-like responses and further analyses reveal a trivial multiband origin and at least two bands contributing to the transport. The conclusion is well supported by the first-principles calculations. We hence understand that the finite T_p is a natural result due to temperature dependent scattering time and chemical potentials in degenerately doped narrow-gap semiconductors.

We first introduce the dual-gated electric field effect measured at T = 1.7 K in Fig. 1. The longitudinal sheet resistance R_{sq} ($R_{sq} = \frac{L}{W}R_{xx}$, with L and W being the channel length and width, respectively) at zero magnetic field (Fig. 1c upper panel) and anti-symmetrized Hall resistance $R_{xy} = \frac{R_{xy}(B = 1\ T) - R_{xy}(B = -1\ T)}{2}$ at a magnetic field B = 1 T (Fig. 1c lower panel) are presented as functions of the top and bottom gate voltages (V_{tg} and V_{bg}) in color contour plots. The R_{sq} reaches a global maximum at small values of (V_{tg}, V_{bg}) = (0.40 V, 0.40 V), which corresponds to the chemical potential tuned to the charge neutrality point (CNP). It is also evidenced by the sign reversal of the Hall resistance near the same point.

The linecuts along the off-diagonal dashed white lines (corresponding to equal densities induced by the two gates) of the two color maps in Fig. 1c are shown in the upper panel of Fig. 1d. The device exhibits graphene-like ambipolar electrical field effect with CNP at V_D = 0.40 V and a large on/off ratio about 40[32, 33]. Both the conductance $\sigma_{xx} = 1/R_{sq}$ and the inverse of Hall resistance $1/R_{xy}$ increases linearly on the p-doped ($V_{tg} < V_D$) and n-doped ($V_{tg} > V_D$) sides of V_D, indicating effective tunning of the charge transport and carrier densities (Fig. 1d lower panel). The Hall mobility can be extracted by $\mu_H = \sigma_{xx}R_H^l$, where $R_H^l \approx R_{xy}/B$ is the low-field Hall coefficient for $B < 0.5$ T. We obtain $\mu_H = \sim 8{,}000\ cm^2V^{-1}s^{-1}$ and $\sim 5{,}000\ cm^2V^{-1}s^{-1}$ for the n-type and p-type charge carriers, respectively. The quantum oscillations due to the Landau level formation have also been observed and shown in Fig. S7 of SI, indicating high quality of our device. While in early attempts of obtaining thin $ZrTe_5$ flakes, the device mobility is usually much lower and the gate

tuning is inefficient (ionic gating[29] or SiO_2 gate[23, 28, 30]). Our results indicate that the hBN encapsulation greatly helps maintain the high quality of $ZrTe_5$ crystals and prevent sample degradation that can hardly be avoided by other fabrication methods in previous experiments[28-30]. Note that the gate voltages are applied symmetrically to maintain $C_{tg}(V_{tg}-V_D)=C_{bg}(V_{bg}-V_D)$ throughout the following part of the paper while only the V_{tg} is labeled for simplification.

With the gate-tunability established, we now attempt to resolve the mystery of "resistance peak" by performing temperature dependent measurements at controlled densities. The curves of $R_{sq}(T)$ at different gate voltages (selected along the dashed line in Fig. 1c) are plotted in Fig. 2, displaying resistance maxima at temperatures denoted as T_p (highlighted by the vertical short markers). In general, the device exhibits insulating behaviors ($\frac{dR_{sq}}{dT} < 0$) at $T > T_p$ and metallic behaviors ($\frac{dR_{sq}}{dT} > 0$) at $T < T_p$. When the chemical potential is tuned close to the CNP ($V_{t(b)g} = V_D = 0.40$ V), $R_{sq}(T)$ keeps increasing upon cooling and T_p is nearly suppressed to the lowest temperature. A thermal activation gap Δ ~40 meV is extracted from the Arrhenius fit of $R_{sq} \sim \exp\left(\frac{\Delta}{k_B T}\right)$ at the CNP (see Fig. S6 in SI). When the gate voltages are tuned away from the CNP, T_P shifts to higher temperatures and the peak resistance deceases, as guided by the grey dashed curve in the electron-doped side ($V_{t(b)g} > V_D$) and red dashed curve in the hole-doped side ($V_{t(b)g} < V_D$). The trend reminds us of the temperature-dependent resistivity observed in $ZrTe_5$ bulk crystals grown by different methods. The T_P typically falls into a range between 120 -180 K for the bulk samples grown by the chemical vapor transport (CVT) method[4-7, 9, 12, 13, 20, 26, 30, 34-44], while being smaller than 100 K for the flux-method grown samples (some have $T_p \approx 0$)[2-4, 14, 21-26, 43, 45-48]. The flux samples are believed to have less Te vacancies and smaller densities comparing to the CVT samples. Surprisingly, the feature of $R_{sq}(T)$ in different bulk samples can be realized in one single gate-tunable device here. We also observe asymmetry in the gate dependence of the resistance peaks on the two sides away from the CNP. On the hole doped side with increasing the doping density, the T_p shifts to higher temperature in a faster fashion and the resistance peak decreases more substantially.

In order to better understand the above features, we have performed Hall measurements at different doping levels and temperatures. The temperature induced evolution of the Hall resistances at three representative gate voltages, V_{tg} = -0.75 V (hole-doped side), 0.40 V (charge neutrality), and 1.20 V (electron-doped side), are shown in Fig. 3a. Negative slopes of the Hall resistance are always observed at V_{tg} = -0.75 V, regardless of the temperature being below or above T_p (~200 K, see the green curve in Fig. 2), indicating the hole dominance of the charge transport. In contrast, at V_{tg} = 0.40 V and 1.20 V, stronger nonlinearity has been observed for the Hall resistances. With increasing temperature, the low-field ($B \sim 0$ T) Hall coefficient ($\frac{dR_{xy}}{dB}$)

changes sign, followed by another "sign reversal" of the high-field (B ~ 9 T) Hall coefficient at higher temperatures.

We extract the two Hall coefficients (denoted as $R_{\mathrm{H}}^{\mathrm{l}}$ and $R_{\mathrm{H}}^{\mathrm{h}}$, respectively) and plot them as functions of temperature for the three gate voltages in Fig. 3b. Examples of extracting $R_{\mathrm{H}}^{\mathrm{l}}$ (slope of the red dashed lines) and $R_{\mathrm{H}}^{\mathrm{h}}$ (slope of the grey dashed lines) at T = 150 K are shown in the insets. Again, smaller inconsistency between the $R_{\mathrm{H}}^{\mathrm{l}}$ and $R_{\mathrm{H}}^{\mathrm{h}}$ is observed in the hole-doped side (V_{tg} = -0.75 V) and they only decrease (in magnitude) slightly with increasing temperature. While at V_{tg} = 0.40 V and 1.20 V, the low-field (B ~ 0 T) Hall coefficient $R_{\mathrm{H}}^{\mathrm{l}}$ quickly changes sign at ~50 K and ~120 K, respectively. The high-field Hall coefficient $R_{\mathrm{H}}^{\mathrm{h}}$ is typically a measure of the total carrier density of the system (in the semiclassical transport limit of $\mu B \gg 1$, with μ being the effective carrier mobility), supported by its nearly constant value at low temperatures (< ~150 K). We note that the "sign reversal" of $R_{\mathrm{H}}^{\mathrm{h}}$, which is extracted near 9 T, does not necessarily indicate a change in the total carrier density at high temperatures (150 ~ 200 K, where μ is less than ~200 cm^2/Vs). The reasoning is further explored in SI. We notice that at the electron-doped side (V_{tg} = 1.20 V), the resistance peak happening at $T_{\mathrm{p}} \approx$ ~120 K (see Fig. 2) seems to correlate with the sign reversal of the low-field Hall coefficient ($R_{\mathrm{H}}^{\mathrm{l}}$), consistent with that observed in bulk crystals[4, 12, 19-21, 26, 37]. However, on the hole-doped side, the resistance peaks still emerge even without any sign change of the Hall resistances.

The nonlinearity of the Hall resistance observed in $ZrTe_5$ has been previously attributed to the anomalous Hall effect (AHE)[22, 23, 25, 49-51], the multi-band transport[2, 7, 14, 21, 26, 27, 29, 36, 37, 52], or the thermally excited two carriers [4, 18, 53]. Step-like Hall resistances can be obtained by subtracting $R_{\mathrm{H}}^{\mathrm{h}}B$ from the total Hall resistances at T = 1.7 K (Fig. 4a), resembling the anomalous Hall effect observed in soft ferromagnetic conductors[54]. Although, the presence of AHE can give rise to the nonlinearity of the Hall resistance, we note that it is unlikely to explain the observation in our devices. The majority of recent experimental and theoretical studies suggest $ZrTe_5$ to have a bulk band gap (varying from ~6 -100 meV) [20, 35, 43, 55-58]. In one scenario, the AHE can result from the formation of Weyl nodes, which are sources and sinks of Berry flux, with the inversion of the conduction and valence bands (CB and VB) upon applying external magnetic fields[22, 51]. It requires the Zeeman energy $g\mu_{\mathrm{B}}B$ (g is the Landé g-factor) to exceed the band gap. Taking a relatively large $g \approx 21$ [37] and the estimated energy gap from $2\Delta \approx 80$ meV (twice the activation gap), we can approximately evaluate the critical magnetic field to be larger than 65 T, which is far beyond the value we applied here.

Another mechanism of generating non-zero Berry curvature is from the magnetic-field-induced spin splitting of the massive Dirac bands (schematics shown in the inset of Fig. 4b)[23, 25, 49, 50]. It gives rise to the AHE which saturates when the chemical potential only crosses one spin-split band. Hence the saturation field B_0 is Fermi energy (E_F) dependent. Based on the calculated energy dispersion of bulk $ZrTe_5$, we estimate B_0 from $B_0 \propto E_F \propto n^{2/3}$ (illustrated by the grey curve in Fig. 4b)[50], which exhibits strong density dependence and quickly becomes larger than ~30 T for the carrier density $n > \sim 10^{18}$ cm^{-3}. Experimentally, the saturation field B_0 can be extracted from the crossing point of the two dashed lines (tracing the low-field and high-field Hall slopes, respectively) at different doping levels (see examples in Fig. 4a), showing a trend of saturation with much smaller values as the chemical potential moves away from the CNP (Fig. 4b). The observation in our experiment is apparently inconsistent with the AHE induced from Zeeman splitting of the massive Dirac band.

The other likely cause of nonlinearity in the Hall signal is the multiband transport[37, 52]. As shown in Fig. 4c, we attempt to use the semiclassical two-band model to fit the experimental Hall curves (T = 1.7 K) at different total densities (details in SI)[14, 21, 26, 27, 36, 52]. This rather simplified model gives reasonably good fitting results (as shown by the dashed curves) for almost all the Hall resistances. The extracted carrier densities (n_1, n_2, and $n_1 + n_2$), mobilities (μ_1 and μ_2), and corresponding ratios (n_2/n_1 and μ_1/μ_2) are plotted as functions of the total density n in Fig. 4d-4f. The transport can then be classified into the contribution from one band with lower densities and higher mobilities (n_1 and μ_1), and the other band with higher densities and lower mobilities (n_2 and μ_2). The electron mobility of band 1 is as high as ~15,000 cm^{2}V^{-1}s^{-1}. The n_1 and n_2 (black and red symbols in the top panel of Fig. 4d) are almost linearly tuned by the electrostatic gates, both changing their sign near the CNP. Their sum $n_1 + n_2$ (blue symbols) shows general agreement with the total carrier density n calculated from the geometric capacitances and the gate voltages, supporting the validity of our fittings. The difference of $\mu_{1,2}$ at $n > 0$ and $n < 0$ indicates electron-hole asymmetries. The $n_2/n_1 > 1$ indicates band 2 is heavier than band 1 (effective mass $m^*_{1,2} \propto n^{2/3}_{1,2}$) and the difference is more apparent in the electron-doped side (see Fig. 4f).

The multiband nature of $ZrTe_5$ is also revealed by our first-principles calculations (Fig. 5a and 5b, see more details in Methods) as well as some other studies[25, 26, 52]. We obtain a ~70 meV bandgap, near which multiple electron and hole pockets can be identified (Fig. 5b). The shapes of the bands near the band edges are also very different for the CB and VB, contributing to the different transport properties (electron-hole asymmetry). Comparing with the above results from the two-band fittings of the Hall curves, the band 1 with higher mobilities and smaller effective masses should arise from the Dirac-like band near the Γ point, while the band 2 represents the averaged contribution from the other bands. We have also calculated the

resistivity as a function of temperature at a few fixed total densities using the BoltzTrap code[59]. For simplicity, we only consider the scattering time τ dominated by the electron-phonon interaction in which τ is proportional to $1/T$ and assume five times larger τ for the holes (the assumption is validated as shown by our scattering analyses in SI). As shown in Fig. 4c, the main resistivity behaviors can be reproduced, such as the resistivity peak and its shifting with increasing the electron or hole densities[26]. The temperatures for the resistivity peaks are plotted in Fig. 5d, showing general consistency with the experimental T_p values extracted from Fig. 2. The small deviation should result from the oversimplified model, in which we only considered electron-phonon as the main scattering source and assume constant ratio of the scattering times between electron and hole bands. The dispersion of T_p divide the T - n map into three regions, corresponding to the p-type metal ($T < T_P$ and $V_{tg} < V_D$), n-type metal ($T < T_P$ and $V_{tg} > V_D$), and p-type semiconductor ($T > T_P$), respectively. The schematic electronic dispersion with two sets of bands and the corresponding Fermi energies are illustrated for each region. Upon increasing the temperature, the chemical potential $\tilde{\mu}(T)$ approaches the intrinsic Fermi level, which is inferred to be closer the VB maxima due to the lighter effective masses.

We also note that the occurrence of the resistivity peak is a natural result in degenerate semiconductors with narrow gaps. The essence can be captured by a simplified model with even only considering one set of conduction and valence bands (detailed calculation and discussion can be found in SI). Further considering the difference in scattering time in the CB and VB will reproduce the T_p difference in for the electron and hole-doped sides (Fig. S11). The temperature induced change of $\tilde{\mu}(T)$ is also in good agreement with the results reported previously: it tends to shift upward [35, 60] from the VB or shifts downward [19, 20, 61] from the CB when the temperature increases. In conventional metals with large Fermi energy, the chemical potential $\tilde{\mu}$ does not change appreciably since $k_B T \ll E_F$. However, in degenerate semiconductor with narrow-gap or semimetals, where the VB maximum and CB minimum are in proximity (few tens of meV) to the chemical potential, significant shifting of the chemical potential with temperature can happen [53, 62, 63].

In summary, we have investigated the multiband properties of $ZrTe_5$ thin flakes by systematic gating and temperature dependent transport measurements. The temperature of the resistance peaks (T_P) and nonlinearity of Hall resistance can be efficiently tuned by the gate voltages, through which we identify a multiband origin and the highly asymmetric CB and VB dispersions with narrow bandgaps. Though exotic mechanisms like TPT or interaction effects cannot be fully excluded for the resistance anomaly in bulk $ZrTe_5$ [6, 7, 11, 18], our results provide a crucial step toward understanding its peculiar transport behaviors and paves the way for further exploring topological properties in thin $ZrTe_5$ devices.

Note

The authors declare no competing financial interest.

Acknowledgement

This work was supported by the National Natural Science Foundation of China (Grants No. 12174439, 11961141011, 12274436, and 12188101), the Strategic Priority Research Program of Chinese Academy of Sciences (Grant No. XDB28000000), the National Key Research and Development Program of China (Grant No. 2021YFA1401300 and 2022YFA1403403). Work at Brookhaven National Laboratory was supported by the U.S. Department of Energy, Office of Science, Office of Basic Energy Sciences, under Contract No. DE-SC0012704. The growth of hBN crystals was supported by the Elemental Strategy Initiative of MEXT, Japan, and CREST (JPMJCR15F3), JST.

Supporting Information

Further details of the device fabrication, transport measurement setup, theoretical calculation methods, magnetotransport data analysis, scatterings mechanisms, two-band model for fitting the Hall resistances, temperature-dependent resistivity from a simplified narrow-gap model, and additional datasets for supporting the conclusion in the main text.

Reference

(1) Weng, H.; Dai, X.; Fang, Z. Transition-Metal Pentatelluride ZrTe5 and HfTe5: A Paradigm for Large-Gap Quantum Spin Hall Insulators. *Physical Review X* **2014**, *4* (1), 011002.

(2) Zhang, W.; Wang, P.; Skinner, B.; Bi, R.; Kozii, V.; Cho, C. W.; Zhong, R.; Schneeloch, J.; Yu, D.; Gu, G.; et al. Observation of a thermoelectric Hall plateau in the extreme quantum limit. *Nat Commun* **2020**, *11* (1), 1046.

(3) Li, Q.; Kharzeev, D. E.; Zhang, C.; Huang, Y.; Pletikosić, I.; Fedorov, A. V.; Zhong, R. D.; Schneeloch, J. A.; Gu, G. D.; Valla, T. Chiral magnetic effect in ZrTe5. *Nature Physics* **2016**, *12* (6), 550-554.

(4) Tang, F.; Ren, Y.; Wang, P.; Zhong, R.; Schneeloch, J.; Yang, S. A.; Yang, K.; Lee, P. A.; Gu, G.; Qiao, Z.; et al. Three-dimensional quantum Hall effect and metal-insulator transition in ZrTe5. *Nature* **2019**, *569* (7757), 537-541.

(5) Zhang, J. L.; Guo, C. Y.; Zhu, X. D.; Ma, L.; Zheng, G. L.; Wang, Y. Q.; Pi, L.; Chen, Y.; Yuan, H. Q.; Tian, M. L. Disruption of the Accidental Dirac Semimetal State in ZrTe5 under Hydrostatic Pressure. *Phys Rev Lett* **2017**, *118* (20), 206601.

(6) Xu, B.; Zhao, L. X.; Marsik, P.; Sheveleva, E.; Lyzwa, F.; Dai, Y. M.; Chen, G. F.; Qiu, X. G.; Bernhard, C. Temperature-Driven Topological Phase Transition and Intermediate Dirac Semimetal Phase in ZrTe5. *Phys Rev Lett* **2018**, *121* (18), 187401.

(7) Tian, Y.; Ghassemi, N.; Ross, J. H. Dirac electron behavior and NMR evidence for topological band inversion in ZrTe5. *Physical Review B* **2019**, *100* (16), 165149.

(8) Vaswani, C.; Wang, L. L.; Mudiyanselage, D. H.; Li, Q.; Lozano, P. M.; Gu, G.; Cheng, D.; Song, B.; Luo, L.; Kim, R. H. J.; et al. Light-Driven Raman Coherence as a Nonthermal Route to Ultrafast Topology Switching in a Dirac Semimetal. *Physical Review X* **2020**, *10* (2), 021013

(9) Zhou, Y.; Wu, J.; Ning, W.; Li, N.; Du, Y.; Chen, X.; Zhang, R.; Chi, Z.; Wang, X.; Zhu, X.; et al. Pressure-induced superconductivity in a three-dimensional topological material ZrTe5. *Proc Natl Acad Sci* **2016**, *113* (11), 2904-2909.

(10) Jiang, Y. Z., Tianhao ; Zhang, Luojia ; Chen, Qiang ; Zhou, Haidong ; Ozerov, Mykhaylo ; Smirnov, Dmitry ; Jiang, Zhigang. Anomalous temperature evolution of the Dirac band in ZrTe5 across topological phase. **2022**, *arXiv:2101.02681*. arXiv.org e-Print achive. https://arxiv.org/abs/2211.16711 (acccessed May 16, 2023).

(11) Mohelsky, I.; Wyzula, J.; Piot, B. A.; Gu, G. D.; Li, Q.; Akrap, A.; Orlita, M. Temperature dependence of the energy band gap in ZrTe5: Implications for the topological phase. *Physical Review B* **2023**, *107* (4), L041202.

(12) Jones, T. E.; Fuller, W. W.; Wieting, T. J.; Levy, F. Thermoelectric power of HfTe5 and ZrTe5. *Solid State Communications* **1982**, *42* (11), 793-798.

(13) Okada, S.; Sambongi, T.; Ido, M. Giant Resistivity Anomaly in ZrTe5. *Journal of the Physical Society of Japan* **1980**, *49* (2), 839-840.

(14) Wang, H.; Liu, H.; Li, Y.; Liu, Y.; Wang, J.; Liu, J.; Dai, J. Y.; Wang, Y.; Li, L.; Yan, J.; et al. Discovery of log-periodic oscillations in ultraquantum topological materials. *Sci Adv* **2018**, *4* (11), eaau5096.

(15) Okada, S.; Sambongi, T.; Ido, M.; Tazuke, Y.; Aoki, R.; Fujita, O. Negative Evidences for Charge/Spin Density Wave in ZrTe5. *Journal of the Physical Society of Japan* **1982**, *51* (2), 460-467.

(16) DiSalvo, F. J.; Fleming, R. M.; Waszczak, J. V. Possible phase transition in the quasi-one-dimensional materials ZrTe5 or HfTe5. *Physical Review B* **1981**, *24* (6), 2935-2939.

(17) Rubinstein, M. HfTe5 and ZrTe5: Possible polaronic conductors. *Physical Review B* **1999**, *60* (3), 1627-1632.

(18) Fu, B.; Wang, H. W.; Shen, S. Q. Dirac Polarons and Resistivity Anomaly in ZrTe5 and HfTe5. *Phys Rev Lett* **2020**, *125* (25), 256601.

(19) McIlroy, D. N.; Moore, S.; Zhang, D.; Wharton, J.; Kempton, B.; Littleton, R.; Wilson, M.; Tritt, T. M.; Olson, C. G. Observation of a semimetal–semiconductor phase transition in the intermetallic ZrTe5. *Journal of Physics: Condensed Matter* **2004**, *16* (30), L359-L365.

(20) Zhang, Y.; Wang, C.; Yu, L.; Liu, G.; Liang, A.; Huang, J.; Nie, S.; Sun, X.; Zhang, Y.; Shen, B.; et al. Electronic evidence of temperature-induced Lifshitz transition and topological nature in ZrTe5. *Nat Commun* **2017**, *8*, 15512.

(21) Chi, H.; Zhang, C.; Gu, G.; Kharzeev, D. E.; Dai, X.; Li, Q. Lifshitz transition mediated electronic transport anomaly in bulk ZrTe5. *New Journal of Physics* **2017**, *19* (1), 015005.

(22) Liang, T.; Lin, J.; Gibson, Q.; Kushwaha, S.; Liu, M.; Wang, W.; Xiong, H.; Sobota, J. A.; Hashimoto, M.; Kirchmann, P. S.; et al. Anomalous Hall effect in ZrTe5. *Nature Physics* **2018**, *14* (5), 451-455.

(23) Mutch, J.; Ma, X.; Wang, C.; Malinowski, P.; Ayres-Sims, J.; Jiang, Q.; Liu, Z.; Xiao, D.; Yankowitz, M.; Chu, J.-H. Abrupt switching of the anomalous Hall effect by field-rotation in nonmagnetic ZrTe5. **2021**, *arXiv:2101.02681*. arXiv.org e-Print achive. https://arxiv.org/abs/2101.02681 (acccessed May 16, 2023).

(24) Wang, Y.; Legg, H. F.; Bomerich, T.; Park, J.; Biesenkamp, S.; Taskin, A. A.; Braden, M.; Rosch, A.; Ando, Y. Gigantic Magnetochiral Anisotropy in the Topological Semimetal ZrTe5. *Phys Rev Lett* **2022**, *128* (17), 176602.

(25) Sun, Z.; Cao, Z.; Cui, J.; Zhu, C.; Ma, D.; Wang, H.; Zhuo, W.; Cheng, Z.; Wang, Z.; Wan, X.; et al. Large Zeeman splitting induced anomalous Hall effect in ZrTe5. *npj Quantum Materials* **2020**, *5* (1), 36.

(26) Shahi, P.; Singh, D. J.; Sun, J. P.; Zhao, L. X.; Chen, G. F.; Lv, Y. Y.; Li, J.; Yan, J. Q.; Mandrus, D. G.; Cheng, J. G. Bipolar Conduction as the Possible Origin of the Electronic Transition in Pentatellurides: Metallic vs Semiconducting Behavior. *Physical Review X* **2018**, *8* (2), 021055.

(27) Lu, J.; Zheng, G.; Zhu, X.; Ning, W.; Zhang, H.; Yang, J.; Du, H.; Yang, K.; Lu, H.; Zhang, Y.; et al. Thickness-tuned transition of band topology in ZrTe5 nanosheets. *Physical Review B* **2017**, *95* (12), 125135.

(28) Xie, Z. J.; Wei, X. J.; Cao, S. M.; Zhang, Y.; Yan, S. L.; Gu, G. D.; Li, Q.; Chen, J. H. Electron-electron interactions and weak antilocalization in few-layer ZrTe5 devices. *Physical Review B* **2021**, *103* (15), 155408.

(29) Niu, J.; Wang, J.; He, Z.; Zhang, C.; Li, X.; Cai, T.; Ma, X.; Jia, S.; Yu, D.; Wu, X. Electrical transport in nanothick ZrTe5 sheets: From three to two dimensions. *Physical Review B* **2017**, *95* (3), 035420.

(30) Tang, F.; Wang, P.; Wang, P.; Gan, Y.; Wang, L.; Zhang, W.; Zhang, L. Multi-carrier transport in ZrTe5 film. *Chinese Physics B* **2018**, *27* (8), 087307.

(31) Tang, F.; Wang, P.; He, M.; Isobe, M.; Gu, G.; Li, Q.; Zhang, L.; Smet, J. H. Two-Dimensional Quantum Hall Effect and Zero Energy State in Few-Layer ZrTe5. *Nano Lett* **2021**, *21* (14), 5998-6004.

(32) Zhang, Y.; Tan, Y. W.; Stormer, H. L.; Kim, P. Experimental observation of the quantum Hall effect and Berry's phase in graphene. *Nature* **2005**, *438* (7065), 201-204.

(33) Novoselov, K. S.; Geim, A. K.; Morozov, S. V.; Jiang, D.; Katsnelson, M. I.; Grigorieva, I. V.; Dubonos, S. V.; Firsov, A. A. Two-dimensional gas of massless Dirac fermions in graphene. *Nature* **2005**, *438* (7065), 197-200.

(34) Li, P.; Zhang, C. H.; Zhang, J. W.; Wen, Y.; Zhang, X. X. Giant planar Hall effect in the Dirac semimetal ZrTe5−δ. *Physical Review B* **2018**, *98* (12), 121108.

(35) Wu, R.; Ma, J. Z.; Nie, S. M.; Zhao, L. X.; Huang, X.; Yin, J. X.; Fu, B. B.; Richard, P.; Chen, G. F.; Fang, Z.; et al. Evidence for Topological Edge States in a Large Energy Gap near the Step Edges on the Surface of ZrTe5. *Physical Review X* **2016**, *6* (2), 021017.

(36) Qiu, G.; Du, Y.; Charnas, A.; Zhou, H.; Jin, S.; Luo, Z.; Zemlyanov, D. Y.; Xu, X.; Cheng, G. J.; Ye, P. D. Observation of Optical and Electrical In-Plane Anisotropy in High-Mobility Few-Layer ZrTe5. *Nano Lett* **2016**, *16* (12), 7364-7369.

(37) Liu, Y.; Yuan, X.; Zhang, C.; Jin, Z.; Narayan, A.; Luo, C.; Chen, Z.; Yang, L.; Zou, J.; Wu, X.; et al. Zeeman splitting and dynamical mass generation in Dirac semimetal ZrTe5. *Nat Commun* **2016**, *7*, 12516.

(38) Stillwell, E. P.; Ehrlich, A. C.; Kamm, G. N.; Gillespie, D. J. Effect of elastic tension on the electrical resistance of HfTe5 and ZrTe5. *Phys Rev B Condens Matter* **1989**, *39* (3), 1626-1632.

(39) Zhang, J. L.; Wang, C. M.; Guo, C. Y.; Zhu, X. D.; Zhang, Y.; Yang, J. Y.; Wang, Y. Q.; Qu, Z.; Pi, L.; Lu, H. Z.; et al. Anomalous Thermoelectric Effects of ZrTe5 in and beyond the Quantum Limit. *Phys Rev Lett* **2019**, *123* (19), 196602.

(40) Wang, J.; Niu, J.; Yan, B.; Li, X.; Bi, R.; Yao, Y.; Yu, D.; Wu, X. Vanishing quantum oscillations in Dirac semimetal ZrTe5. *Proc Natl Acad Sci* **2018**, *115* (37), 9145-9150.

(41) Manzoni, G.; Gragnaniello, L.; Autes, G.; Kuhn, T.; Sterzi, A.; Cilento, F.; Zacchigna, M.; Enenkel, V.; Vobornik, I.; Barba, L.; et al. Evidence for a Strong Topological Insulator Phase in ZrTe5. *Phys Rev Lett* **2016**, *117* (23), 237601.

(42) Zheng, G.; Zhu, X.; Liu, Y.; Lu, J.; Ning, W.; Zhang, H.; Gao, W.; Han, Y.; Yang, J.; Du, H.; et al. Field-induced topological phase transition from a three-dimensional Weyl semimetal to a two-dimensional massive Dirac metal in ZrTe5. *Physical Review B* **2017**, *96* (12), 121401.

(43) Martino, E.; Crassee, I.; Eguchi, G.; Santos-Cottin, D.; Zhong, R. D.; Gu, G. D.; Berger, H.; Rukelj, Z.; Orlita, M.; Homes, C. C.; et al. Two-Dimensional Conical Dispersion in ZrTe5 Evidenced by Optical Spectroscopy. *Physical Review Letters* **2019**, *122* (21), 217402.

(44) Zheng, G. L.; Lu, J. W.; Zhu, X. D.; Ning, W.; Han, Y. Y.; Zhang, H. W.; Zhang, J. L.; Xi, C. Y.; Yang, J. Y.; Du, H. F.; et al. Transport evidence for the three-dimensional Dirac semimetal phase in ZrTe5. *Physical Review B* **2016**, *93* (11), 115414.

(45) Galeski, S.; Ehmcke, T.; Wawrzynczak, R.; Lozano, P. M.; Cho, K.; Sharma, A.; Das, S.; Kuster, F.; Sessi, P.; Brando, M.; et al. Origin of the quasi-quantized Hall effect in ZrTe5. *Nat Commun* **2021**, *12* (1), 3197.

(46) Wang, P.; Cho, C.-w.; Tang, F.; Wang, P.; Zhang, W.; He, M.; Gu, G.; Wu, X.; Shao, Y.; Zhang, L. Giant Nernst effect and field-enhanced transversal zNT in ZrTe5. *Physical Review B* **2021**, *103* (4), 045203.

(47) Galeski, S.; Legg, H. F.; Wawrzynczak, R.; Forster, T.; Zherlitsyn, S.; Gorbunov, D.; Uhlarz, M.; Lozano, P. M.; Li, Q.; Gu, G. D.; et al. Signatures of a magnetic-field-induced Lifshitz transition in the ultra-quantum limit of the topological semimetal ZrTe5. *Nat Commun* **2022**, *13* (1), 7418.

(48) Chen, R. Y.; Zhang, S. J.; Schneeloch, J. A.; Zhang, C.; Li, Q.; Gu, G. D.; Wang, N. L. Optical spectroscopy study of the three-dimensional Dirac semimetal ZrTe5. *Physical Review B* **2015**, *92* (7), 075107.

(49) Lozano, P. M.; Cardoso, G.; Aryal, N.; Gu, G. D.; Tsvelik, A.; Yin, W. G.; Li, Q. Anomalous Hall effect at the Lifshitz transition in ZrTe5. *Physical Review B* **2022**, *106* (8), L081124.

(50) Liu, Y. Z.; Wang, H. C.; Fu, H. X.; Ge, J.; Li, Y. A.; Xi, C. A. Y.; Zhang, J. L.; Yan, J. Q.; Mandrus, D.; Yan, B. H.; et al. Induced anomalous Hall effect of massive Dirac fermions in ZrTe5 and HfTe5 thin flakes. *Physical Review B* **2021**, *103* (20), L201110.

(51) Choi, Y.; Villanova, J. W.; Park, K. Zeeman-splitting-induced topological nodal structure and anomalous Hall conductivity in ZrTe5. *Physical Review B* **2020**, *101* (3), 035105.

(52) Kovács-Krausz, Z.; Tóvári, E.; Nagy, D.; Márffy, A.; Karpiak, B.; Tajkov, Z.; Oroszlány, L.; Koltai, J.; Nemes-Incze, P.; Dash, S. P.; et al. Revealing the band structure of ZrTe5 using multicarrier transport. *Physical Review B* **2023**, *107* (7), 075152.

(53) Wang, C. Thermodynamically Induced Transport Anomaly in Dilute Metals ZrTe5 and HfTe5. *Phys Rev Lett* **2021**, *126* (12), 126601.

(54) Nagaosa, N.; Sinova, J.; Onoda, S.; MacDonald, A. H.; Ong, N. P. Anomalous Hall effect. *Reviews of Modern Physics* **2010**, *82* (2), 1539-1592.

(55) Zhang, P.; Noguchi, R.; Kuroda, K.; Lin, C.; Kawaguchi, K.; Yaji, K.; Harasawa, A.; Lippmaa, M.; Nie, S.; Weng, H.; et al. Observation and control of the weak topological insulator state in ZrTe5. *Nat Commun* **2021**, *12* (1), 406.

(56) Jiang, Y.; Wang, J.; Zhao, T.; Dun, Z. L.; Huang, Q.; Wu, X. S.; Mourigal, M.; Zhou, H. D.; Pan, W.; Ozerov, M.; et al. Unraveling the Topological Phase of ZrTe5 via Magnetoinfrared Spectroscopy. *Phys Rev Lett* **2020**, *125* (4), 046403.

(57) Li, X. B.; Huang, W. K.; Lv, Y. Y.; Zhang, K. W.; Yang, C. L.; Zhang, B. B.; Chen, Y. B.; Yao, S. H.; Zhou, J.; Lu, M. H.; et al. Experimental Observation of Topological Edge States at the Surface Step Edge of the Topological Insulator ZrTe5. *Phys Rev Lett* **2016**, *116* (17), 176803.

(58) Xiong, H.; Sobota, J. A.; Yang, S. L.; Soifer, H.; Gauthier, A.; Lu, M. H.; Lv, Y. Y.; Yao, S. H.; Lu, D.; Hashimoto, M.; et al. Three-dimensional nature of the band structure of ZrTe5 measured by high-momentum-resolution photoemission spectroscopy. *Physical Review B* **2017**, *95* (19), 195119.

(59) Madsen, G. K. H.; Singh, D. J. BoltzTraP. A code for calculating band-structure dependent quantities. *Computer Physics Communications* **2006**, *175* (1), 67-71.

(60) Moreschini, L.; Johannsen, J. C.; Berger, H.; Denlinger, J.; Jozwiack, C.; Rotenberg, E.; Kim, K. S.; Bostwick, A.; Grioni, M. Nature and topology of the low-energy states in ZrTe5. *Physical Review B* **2016**, *94* (8), 081101.

(61) Manzoni, G.; Sterzi, A.; Crepaldi, A.; Diego, M.; Cilento, F.; Zacchigna, M.; Bugnon, P.; Berger, H.; Magrez, A.; Grioni, M.; et al. Ultrafast Optical Control of the Electronic Properties of ZrTe5. *Phys Rev Lett* **2015**, *115* (20), 207402.

(62) Wu, Y.; Jo, N. H.; Ochi, M.; Huang, L.; Mou, D.; Bud'ko, S. L.; Canfield, P. C.; Trivedi, N.; Arita, R.; Kaminski, A. Temperature-Induced Lifshitz Transition in WTe2. *Phys Rev Lett* **2015**, *115* (16), 166602.

(63) Colinge, J. P.; Colinge, C. A. physics of semicondutor devices. Kluwer: 2002; pp 1-40.

Figure

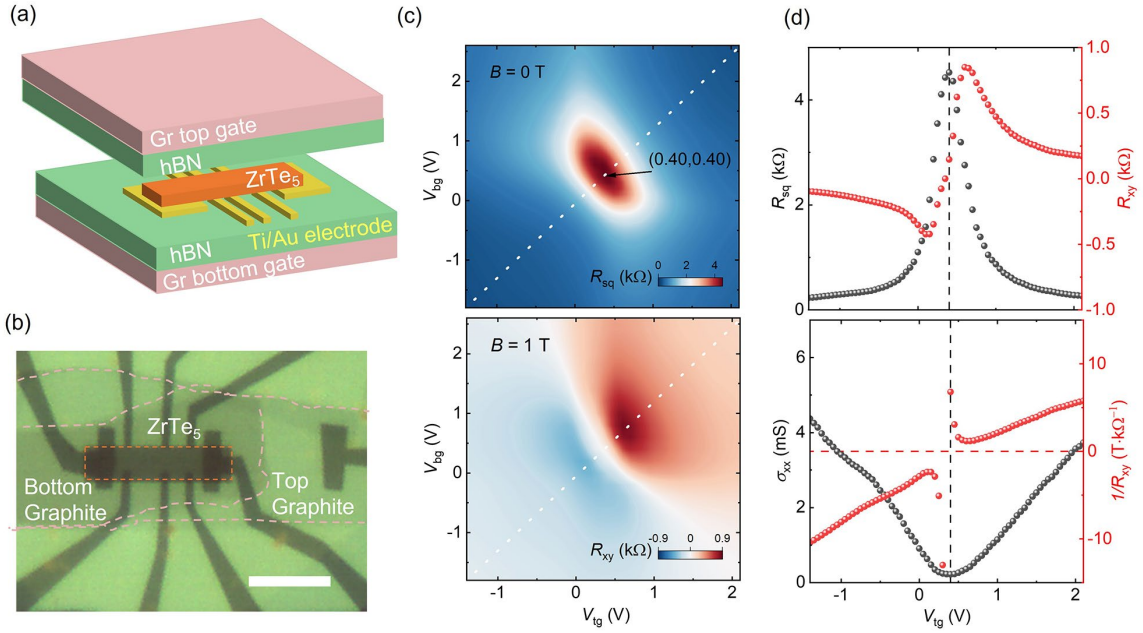

Fig. 1. Device structure and dual-gated field effect of a thin $ZrTe_5$ device. (a, b) Schematic and optical micrograph of the dual-gated thin $ZrTe_5$ (with thickness about 12 nm) Hall-bar device. The scale bar in (b) is 10 μm. (c) Color contour plots of the longitudinal sheet resistance R_{sq} (upper panel $B = 0$ T), and Hall resistance R_{xy} (lower panel, antisymmetrized at $B = \pm 1$ T) as functions of V_{tg} and V_{bg} measured at $T = 1.7$ K, with the corresponding linecuts along the dashed lines (equal density induced by each gate) presented in the upper panel of (d). The arrow in the upper panel of (c) and the vertical dashed lines in (d) highlight the charge neutrality point (CNP). The lower panel in (d) shows the conductance $\sigma_{xx} = 1/R_{sq}$ at $B = 0$ T and the inverse of the Hall resistance $1/R_{xy}$ at $B = 1$ T. Note that the x-axis is labelled as V_{tg} while the V_{bg} (not shown here) is simultaneously tuned according to the dashed line in (c) (same notation is used for the following figures).

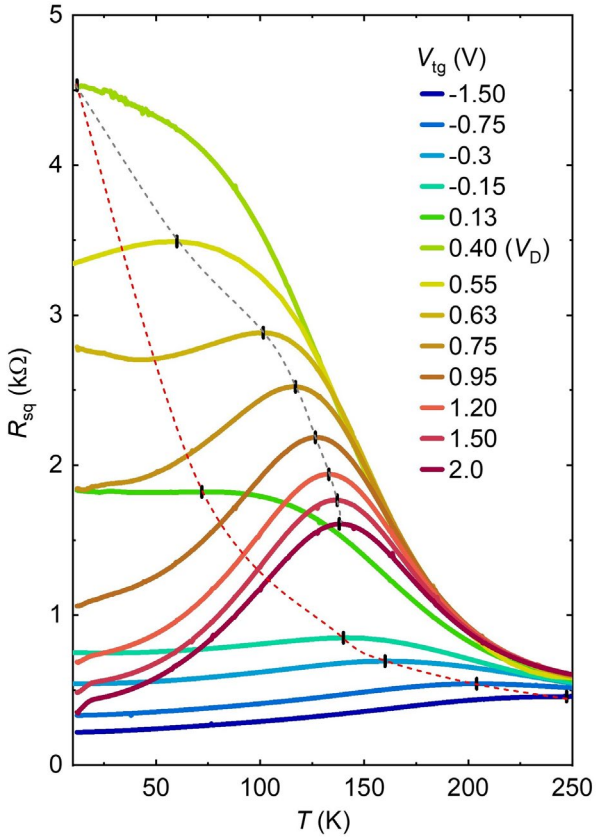

Fig.2. Temperature-dependent resistances and scatterings at a few densities. The $R_{\mathrm{sq}}(T)$ shows pronounced electron-hole asymmetry. The short vertical lines mark the temperature (T_{P}) of the resistance peaks at different gate voltages. The gray and red dashed curves serve as guides to the eye for the tendency of T_{P} at n-doped ($V_{\mathrm{tg}} > 0.40$ V) and p-doped ($V_{\mathrm{tg}} < 0.40$ V) sides, respectively. The data at V_{tg} =-0.30, -0.15, and 0.55 V are extracted from dual-gated resistance mappings at different temperatures.

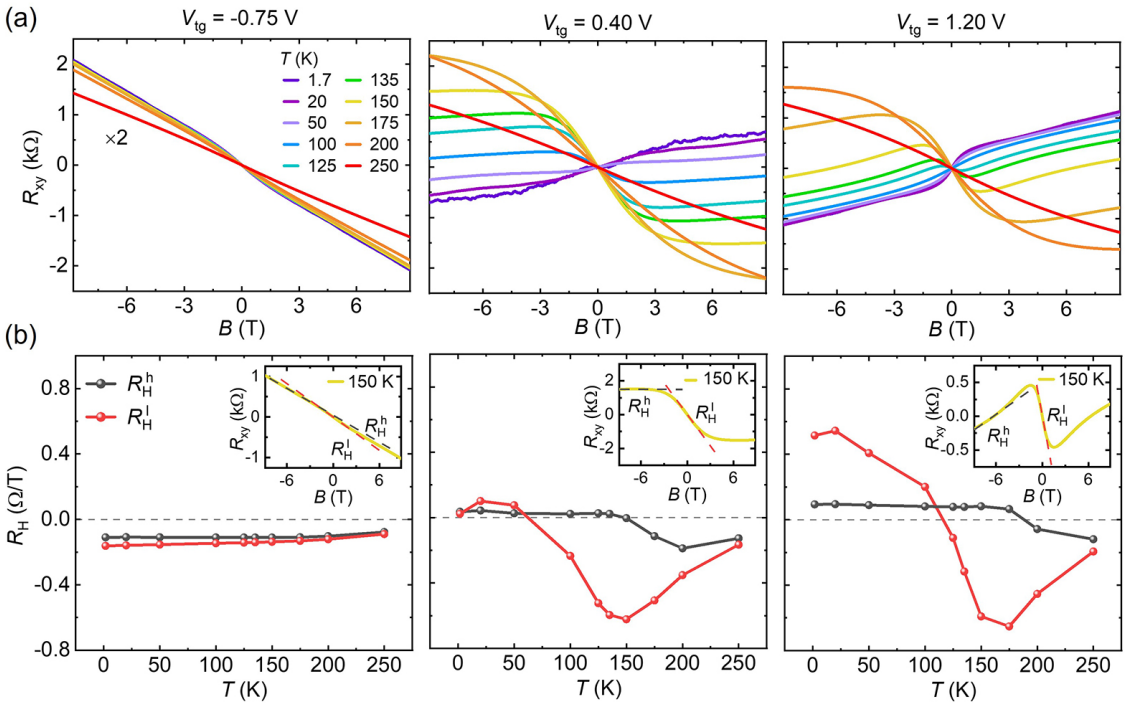

Fig. 3. **Temperature dependence of the Hall measurements at three representative gate voltages.** (a) Temperature-dependent evolution (from 1.7 to 250 K) of the Hall resistance R_{xy} measured at V_{tg} = -0.75 V (hole-doped side), 0.40 V (charge neutrality), and 1.20 V (electron-doped side), respectively. (b) The corresponding Hall coefficients R_H^l (R_H^h) extracted from (a) at low (high) magnetic fields and plotted as functions of temperature. Examples of extracting R_H^l (slope of red dashed line) and R_H^h (slope of gray dashed line) at T = 150 K are shown in the insets. All the plots share the same vertical-axis labeling on the left. The R_{xy} is multiplied by a factor of two for clarity in the left panel of (a).

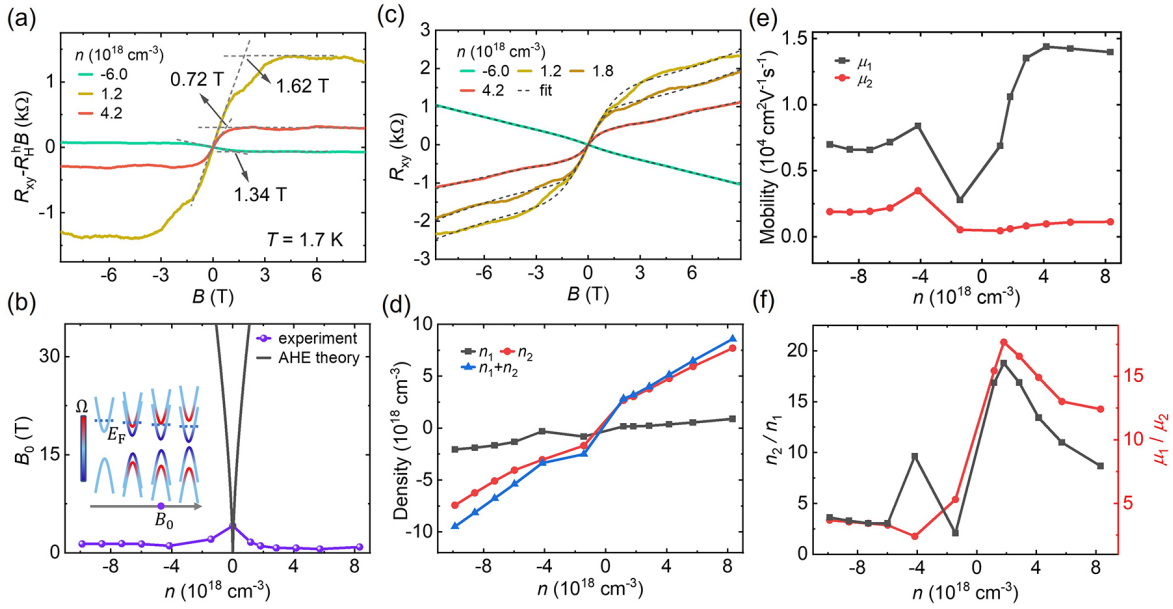

Fig .4. **Multiband induced anomalous-Hall-like response at 1.7 K.** (a) The extracted ($R_{xy} - R_H^h B$) versus B fields for three representative densities (corresponding to n = -6.0, 1.2 and 4.7 ×10^{18} cm^{-3}, respectively), showing anomalous-Hall-like features. We can define a "false" saturation field B_0 at the crossing point of the two dashed lines (tracing the low-field and high-field trends, respectively). (b) The carrier density dependence of B_0 (connected purple symbols), extracted using the method described above. The solid gray curve is the theoretically expected B_0 for the AHE from the Zeeman-split massive Dirac bands (schematic shown in the inset), assuming a relatively large Landé g-factor = 21. (c) The Hall resistance R_{xy} (solid curves) and corresponding two-band-model fittings (dashed curves) at different gate voltages. (d, e) The carrier densities n_i (d) and mobilities μ_i (e) extracted from the two-band-model fittings of the Hall resistances (i = 1, 2). (f) The corresponding ratios (n_2/n_1 and μ_1/μ_2) plotted as functions of the total density n.

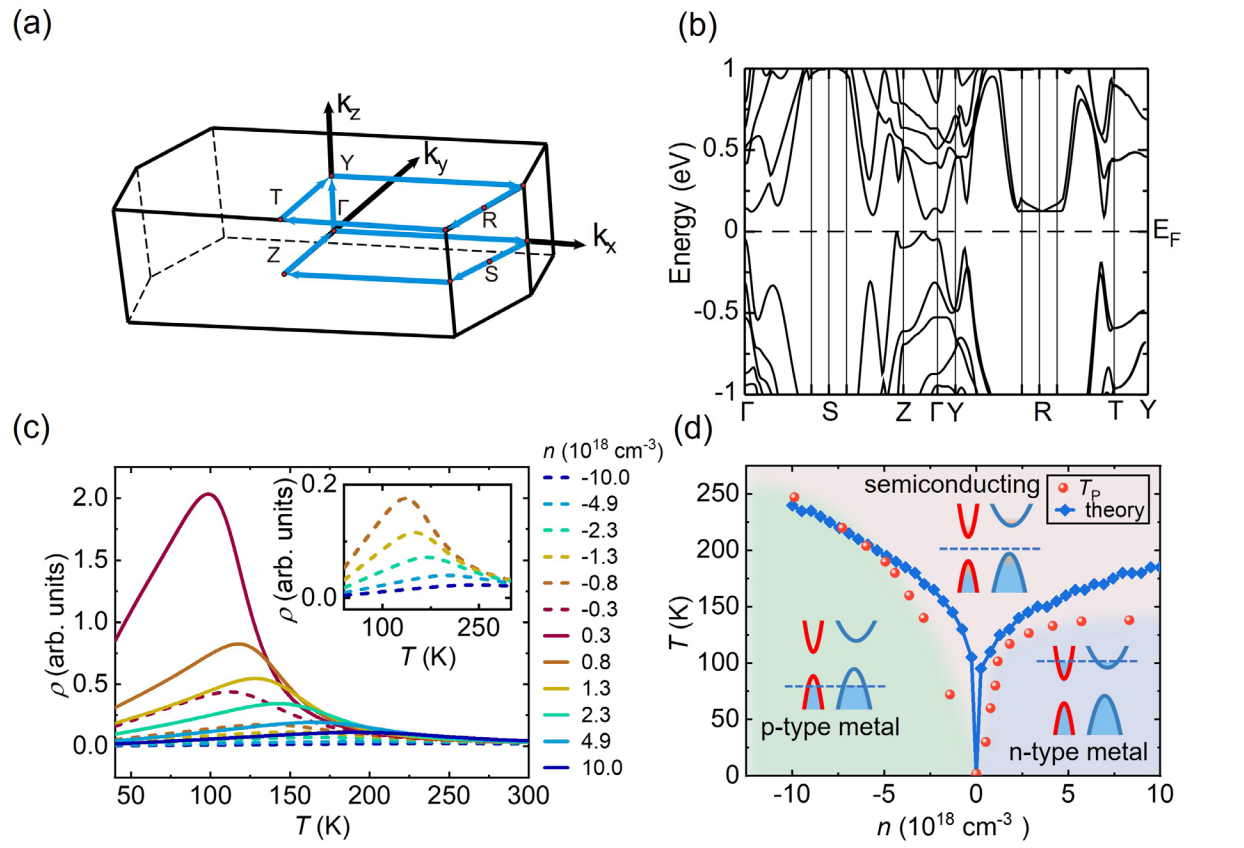

Fig. 5. **Theoretically calculated band structure and transport properties.** (a) The first Brillouin zone with the path (blue arrows) illustrated for the band structure calculation. (b) The band structure for bulk $ZrTe_5$. Note the multiband feature and very different structures of the valence bands and conduction bands. (c) The calculated resistivity ρ as a function of temperature using the Boltztrap code at several carrier densities n. The scattering time τ is assumed five times larger for holes comparing to electrons. The inset shows a zoom-in plot of several most p-doped curves. (d) "Phase diagram" for the $ZrTe_5$ device. The red sphere symbols denote the experimentally extracted T_P, which divides the diagram into three regions: lower-temperature p-type and n-type metallic regime (showing $\frac{dR_{sq}}{dT} > 0$) and higher-temperature semiconducting regime (showing $\frac{dR_{sq}}{dT} < 0$). The boundary is also outlined by the theoretically obtained T_p values (connected bule symbols) extracted from (c). Each region is illustrated with the schematic band structures and corresponding chemical potentials. The red and blue curves denote the lighter and heavier bands, respectively.